Selective Conversion of Syngas to Ethanol over a Tailored Supported RhFe Alloy Catalyst

Wei Zhou,[a] Scott R. Docherty,[a] Erwin Lam,[b] Christian Ehinger,[a] Xiaoyu Zhou,[a] Yuhui Hou,[b] Paco Laveille,[b] and Christophe Copéret*[a]

[a]Department of Chemistry and Applied Bioscience, ETH Zürich, CH-8093 Zürich, Switzerland

[b]Swiss Cat+ East, ETH Zürich, CH-8093 Zürich, Switzerland

*Corresponding author: ccoperet@inorg.chem.ethz.ch

Abstract: The direct conversion of syngas to ethanol is a promising route for the sustainable production of value-added chemicals and fuels. While Fe-promoted Rh-based catalysts have long been studied because of their notable activity and selectivity towards ethanol, the nature of Rh-Fe interaction and the catalyst structure under reaction conditions remain poorly understood due to the complexity of heterogeneous catalysts prepared by conventional approaches. In this work, we construct well-defined RhFe@SiO_2 model catalysts via surface organometallic chemistry (SOMC), composed of small and narrowly distributed nanoparticles supported on silica. Such RhFe@SiO_2 catalyst converts syngas into ethanol, reaching an overall selectivity of 38% ethanol among all products at 8.4% CO conversion, while the non-promoted Rh@SiO_2 catalyst mostly yields methane (selectivity > 90%) and no ethanol. *In situ* X-ray absorption spectroscopy (XAS) reveals that the as-prepared RhFe@SiO_2 and the catalyst under working conditions corresponds to Rh-Fe alloy with ca. 3:1 Rh/Fe ratio dispersed on SiO_2 containing residual Fe^{II} single site. This unique alloyed structure promotes high ethanol selectivity.

Keywords: syngas conversion; ethanol; Fe promoted Rh-based catalysts; SOMC approach; *In situ* XAS

Introduction

Syngas (CO/H_2) serves as a crucial platform for transforming the non-petroleum carbon resources, such as coal, natural gas, shale gas and biomass, into liquid fuels and basic chemicals.[1-3] In that context, major efforts have focused on the direct conversion of syngas into ethanol, an ideal fuel additive, promising hydrogen carrier, and versatile building-block in chemical synthesis.[4-8] Among potential candidates, Rh-based catalysts show promising ethanol selectivity in syngas conversion in the presence of specific additives, so-called promoters.[9-12] Among them, Iron has been shown to be particularly efficient to trigger ethanol production of Rh-based catalysts.[9, 13-17] However, the promotional effect of Fe under syngas conversion conditions remains poorly understood, partly because of the ill-defined catalyst structures resulting from conventional synthetic approaches.

Surface organometallic chemistry (SOMC) has emerged as a powerful synthetic methodology to generate tailored catalysts.[18-20] Specifically, SOMC exploits the surface termination of oxide supports, especially surface OH groups, M_S-OH, to anchor well-defined metal precursors, L_nMX_x through protonolysis, generating atomically dispersed surface species, M_S-O-ML_nX_{x-1} (ca. 1 site/nm^2) while releasing HX. Subsequent thermal treatment under vacuum or reactive atmospheres like H_2 can yield isolated metal sites or nanoparticles with tailored compositions or interfaces. Overall, SOMC generates well-defined models of heterogeneous catalysts, where each component can be selectively introduced and their state probed through detailed characterization. Taken together with catalytic studies and detailed *in situ* or *operando* spectroscopic investigations, molecular-level structure-activity relationships and guideline principles can be elaborated, thus providing opportunities for rational catalyst development. Our group has successfully implemented this approach to explore and understand various heterogeneous catalysts used for propane dehydrogenation,[21,22] selective oxidation of methane [23] and CO_2 hydrogenation.[20,24,25]

Considering the unique ability of Fe to promote the formation of ethanol with Rh-based catalysts, we have thus decided to interrogate the promotional role of Fe in syngas conversion, employing SOMC to prepare well-defined $RhFe@SiO_2$ model catalysts. We find that the introduction of Fe dramatically enhances the activity in syngas conversion and shifts the

product selectivity from almost pure methane to ethanol, along with some amount of methanol. Detailed *in situ* XAS studies demonstrate the formation of RhFe alloyed nanoparticles dispersed on a silica decorated with Fe(II) single sites and shows that the alloy remains under reaction and improve both catalyst activity and ethanol selectivity.

Results and discussion

First, Rh is dispersed via grafting on the residual surface silanols of a silica decorated with isolated Fe^{II}, prepared from the reaction of $Fe_2(OSi(OtBu)_3)_4$ on partially dehydroxylated at 700 °C ($SiO_{2\text{-}700}$) followed by a thermal treatment under vacuum.[26] This tailored support, denoted $Fe^{II}@SiO_2$ and containing ca. 0.9 Fe^{II} nm^{-2} (Figure S1), displays an IR spectrum free of organic ligands, with isolated –OH groups (Figure S2). Upon reaction of Rh(COD)(DIA), a recently developed molecular precursor amenable for grafting,[27] the -OH stretch at 3747 cm^{-1} disappears (Figure 1a), and the resulting material, coined Rh^{I}-$Fe^{II}@SiO_2$, displays peaks at ca. 3250 cm^{-1} (N-H streching), 3100-2700 cm^{-1} (C-H stretching), 1700-1600 cm^{-1} (C=N and C=C stretching), and 1500-1300 cm^{-1} (C-H bending) in the IR spectrum (Figure 1b). These results confirm that the Rh(COD)(DIA) grafts via protonolysis with surface silanols. Subsequent reduction under H_2 at 400 °C yields a black solid, $RhFe@SiO_2$, containing the regenerated Si-OH group but no organic residue. A monometallic $Rh@SiO_2$ is prepared by the same approach using $SiO_{2\text{-}700}$ as previously reported.[27]

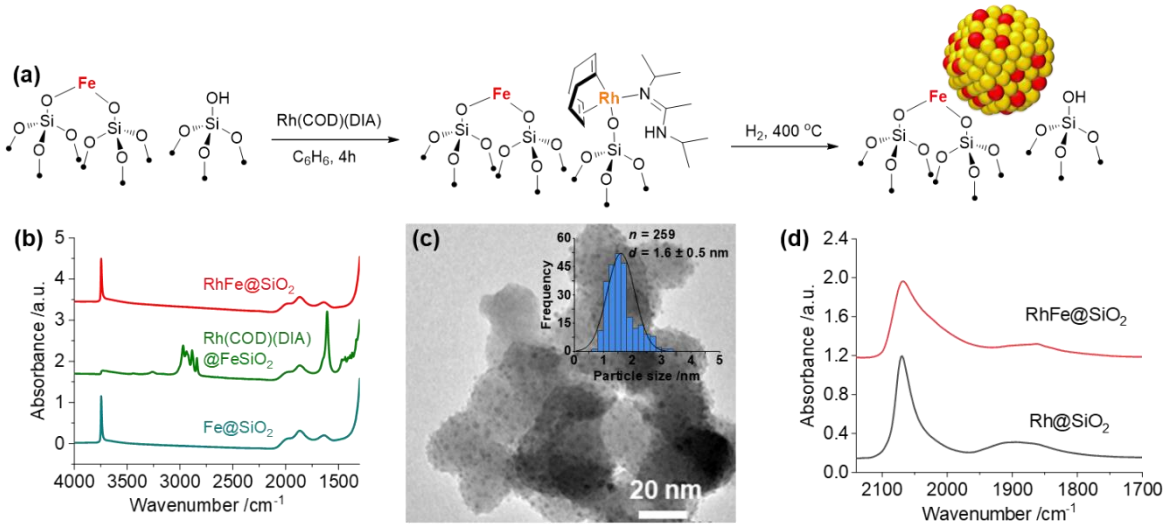

Figure 1. (a) Schematic procedure for grafting of Rh(COD)(DIA) on Fe^{II}@SiO_2 followed by reduction under H_2 at 400 °C. (b) IR spectra throughout the synthesis of RhFe@SiO_2 starting from the second grafting. (c) Particle size distribution and TEM images of RhFe@SiO_2 (d) FTIR spectra of CO adsorbed on Rh@SiO_2 (black line) and RhFe@SiO_2 (red line) under 2.5 mbar CO pressure at room temperature.

Transmission electron microscopy (TEM) shows that RhFe@SiO_2 contains highly-dispersed and small nanoparticles with a narrow particle size distribution (1.6 ± 0.5 nm, Figure 1c). The particle sizes of RhFe@SiO_2 are notably smaller than for the corresponding Rh@SiO_2 (3.3 nm), prepared via the same approach, already indicating a strong interaction between Rh and Fe. FTIR spectra of adsorbed CO shows that two peaks at around 2070 cm^{-1} and 1890 cm^{-1} are both observed over RhFe@SiO_2 and Rh@SiO_2 (Figure 1d); they are assigned to linearly bound CO and bridging CO adsorbed on metallic Rh, respectively. Note that the peak at around 2070 cm^{-1} is significantly broader for RhFe@SiO_2 than for Rh@SiO_2, potentially indicating alloying upon H_2 treatment (*vide infra*).

The as-prepared RhFe@SiO_2 and Rh@SiO_2 catalysts are next evaluated for syngas conversion at 25 bar (H_2/CO/N_2 = 2:1:1.5). Following exposure to air, the catalysts are reduced at 400 °C under H_2 prior to evaluating their performances in syngas conversion. By altering the gas flow rate while fixing the temperature at 250 °C, the RhFe@SiO_2 catalyst provides a high selectivity to CH_3CH_2OH (> 33%) over a wide range of CO conversion (Figure 2a), along with some amount of CH_3OH (around 25%). Notably, the CH_4 and CH_3OH selectivities decrease

with increasing CO conversion, while the opposite trend is observed for ethanol, indicating that C-C coupling is more favorable at longer contact time and ethanol is likely a secondary product. Moreover, study on the effect of temperature indicates that the ethanol selectivity can be slightly increased with increasing in CO conversion, while sacrificing some CH_3OH selectivity. Overall, an ethanol selectivity of up to 38% at 8.4% CO conversion can be obtained at 270 °C (Figure 2b). In contrast, under various conditions, $Rh@SiO_2$ invariably shows inferior CO conversion (< 1%) and high methane selectivity (> 90%) along with small amounts of C_2-C_4 hydrocarbons and no oxygenate organic products (Figure S3 and S4), consistent with previous reports related to non-promoted Rh catalyst for syngas conversion. [16, 28, 29] Note that the catalytic activity of the support – $Fe^{II}@SiO_2$ – for syngas conversion is below detection limit under identical conditions. These findings suggest that the synergy between Rh and Fe is crucial for promoting ethanol formation in syngas conversion.

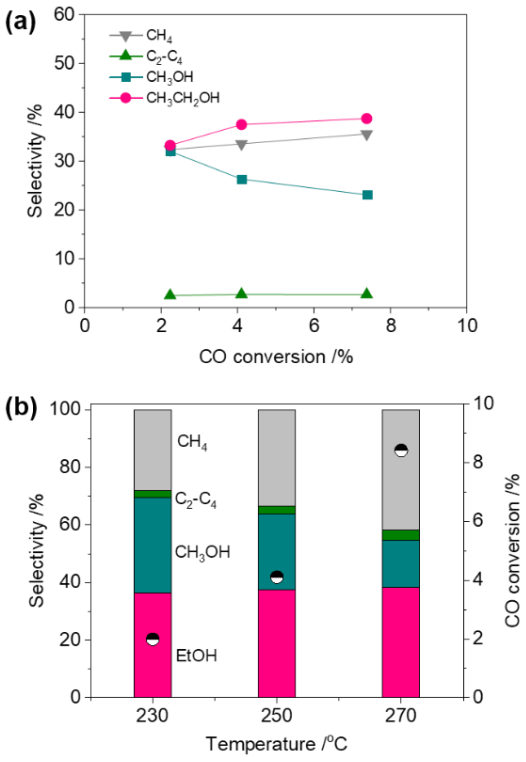

Figure 2. (a) Product selectivity *vs* CO conversion over $RhFe@SiO_2$ catalyst for syngas conversion. Reaction conditions: W_{cat} =50 mg, $CO/H_2/N_2$ = 1:2:1.5, F = 2-8 mL/min, T = 250 °C, P = 25 bar. (b) The effect of temperature on $RhFe@SiO_2$ catalysts. Reaction conditions: W_{cat} =50 mg, $CO/H_2/N_2$ = 1:2:1.5, F = 4 mL/min, T = 230-270 °C, P = 25 bar.

In order to understand the origin of the promotional effect of Fe, we next carried out *in situ* X-ray Absorption Spectroscopy (XAS) experiments to study the structure evolution of RhFe@SiO_2 under different conditions at both the Rh and Fe K-edges (Figure S5). The evolution of structure is first analyzed from Rh K-edge (Figure 3a and 3b), and the fitted values are shown in Figure S6-S9 and summarized in Table S2. The Rh K-edge X-ray absorption near-edge structure (XANES) spectrum of air-exposed RhFe@SiO_2 bears some resemblance to Rh_2O_3 reference (Figure 3a). Simultaneously, two peaks at ~ 1.5 Å and ~ 2.4 Å are observed in the Fourier transform of EXAFS spectra, which are attributed to Rh-O and Rh-Rh scattering path based on the references (Figure 3b). The fitting results reveal that the coordination number (CN) of Rh-Rh and Rh-O are 4.8 and 2.7, respectively (Figure S7 and Table S2). These results suggest that the RhFe@SiO_2 catalyst contains both oxidized and metallic Rh species after exposure to air, which is quite different from what is observed for the monometallic Rh@SiO_2 exposed to air since it contains exclusively metallic Rh (Table S2). [27]

Next, *in situ* X-ray adsorption near-edge structure (XANES) at Rh K-edge are collected to monitor the evolution of air-exposed RhFe@SiO_2 during the H_2 temperature programmed reduction (H_2-TPR) process. The spectra are analyzed using linear combination fitting (LCF) to identify the different Rh species present in the sample. Note that the Rh@SiO_2 is used as the standard Rh metal spectra to minimize the effect of particle size on the XANES spectra (Figure S10). As shown in Figures 3c and 3d, LCF analysis indicates that the air-exposed RhFe@SiO_2 sample can be described as a mixture of ca. 40% Rh_2O_3 and 60% Rh metal. The XANES spectra evolve towards metallic Rh during H_2-TPR, suggesting that the oxidized Rh species in the air-exposed RhFe@SiO_2 can be reversibly reduced. Overall, after H_2 reduction at 400 ^oC, while the peak at ~ 1.5 Å observed in the Fourier transformed EXAFS spectra vanishes (Figure 3b), consistent with the XANES results. The fitting result of EXAFS spectrum show an average CN of 6.8 and 1.7 for Rh-Rh and Rh-Fe respectively (Figure S8 and Table S2), implying the formation of Rh-Fe alloy after H_2 reduction.[16, 30] Wavelet transform (WT) analyses shows a maximum intensity near 9 $Å^{-1}$ and 2.4 Å and a weaker intensity near 5 $Å^{-1}$ and 1.5 Å for air-exposed catalysts, while a maximum intensity near 9 $Å^{-1}$ and 2.4 Å and a weaker intensity near 7 $Å^{-1}$ and 1.9 Å are observed for post H_2 reduction, further indicative of alloy formation (Figure 3e).

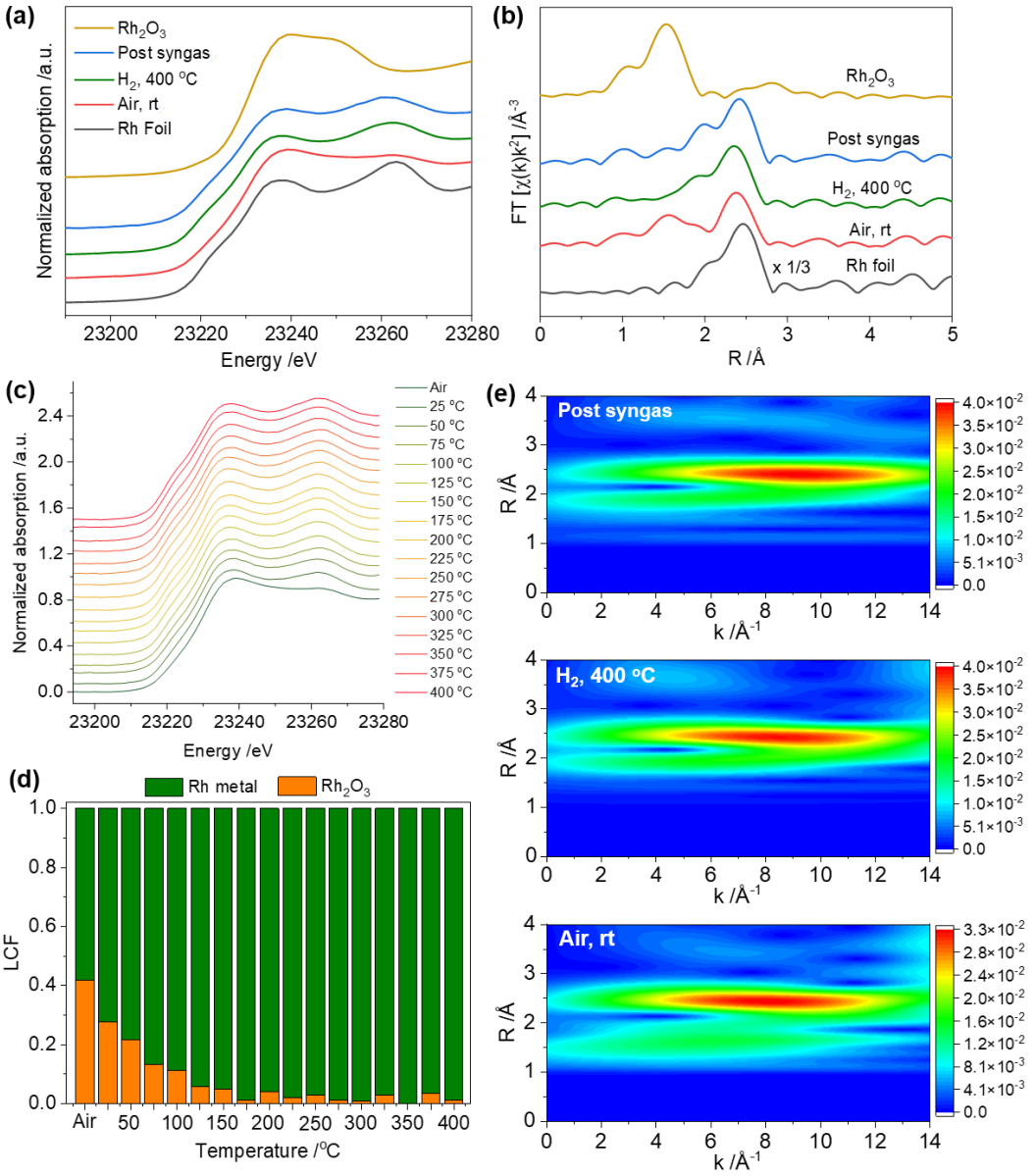

Figure 3. *In situ* XAS of RhFe@SiO_2 at Rh K-edge under different conditions: (a) XANES spectra; (b) the k^2-weighted Fourier transforms of EXAFS spectra; (c) *In situ* XANES collected during H_2 temperature programmed reduction. (d) Results of linear combination fitting (LCF) of Rh K-edge XANES. (e) Wavelet transform analysis of Rh K-edge EXAFS data.

Notably, no change is observed for the XANES during the course of syngas conversion. The fitting of post-syngas EXAFS spectrum indicates similar CN compared to the reduced catalyst (Figure 3a, 3b, Figure S9, S11 and Table S2). Moreover, the wavelet transform (WT) analyses of post-syngas and reduced catalysts are rather similar (Figure 3e). These findings

reveal that alloying persists throughout CO hydrogenation. For the monometallic Rh@SiO_2, it exclusively remains metallic throughout CO hydrogenation (Figure S12 and Table S2), which is well-known for methanation catalysts in syngas conversion. [9]

In situ Fe K-edge XAS spectra under the same conditions are also collected and analyzed to gain more insights into the interplay between Rh and Fe. As shown in Figure 4a, compared to Fe^{II}@SiO_2, the edge position of air-exposed RhFe@SiO_2 shifts to higher position. The intensity of the pre-edge peak at ca. 7113 eV, corresponding to the transition from 1s to 3d-like levels, increases to some extent due to a greater amount of 4p mixing with 3d orbitals when Fe^{II} is oxidized to Fe^{III}. [31] Moreover, the first derivative spectra of air-exposed catalyst significantly shift to higher energy compared to the Fe^{II}@SiO_2 reference (Figure 4b). These results clearly demonstrate that the pristine Fe^{II} was oxidized to Fe^{III} under air-exposed condition. Furthermore, fitting of EXAFS spectrum only shows an average CN of 4.8 for Fe-O scattering contribution in the air-exposed catalyst (Figure 4c, Figure S13, and Table S3).

During H_2-TPR, the intensity of pre-edge gradually decreases and the edge position gradually shifts to a lower energy (Figure S16). These indicate that the oxidized Fe species was reversibly reduced. After H_2 reduction at 400 ^oC, LCF analysis of the Fe K edge XANES spectrum using Fe^{II}@SiO_2 and Fe foil as references demonstrates that ca. 77% Fe is in the state of Fe^{II}@SiO_2, while the remaining 23% Fe is reduced to Fe^0 and is incorporated into the Rh nanoparticle to form the Rh-Fe alloy as discussed above with a Rh/Fe^0 ratio of 3.3:1 (Table S4). Moreover, a new peak at 2.3 Å in R space emerges, which is 0.2 Å higher than that of Fe-Fe scattering path, indicating the absence of Fe aggregation (Figure 4c). The EXAFS fitting results show that this peak belongs to the Fe-Rh scattering path with an average CN of 0.5, which is in accordance with the results from Rh K-edge (Figure S14 and Table S3). Similar to what is observed from Rh K-edge, no changes are observed at the Fe K-edge during syngas conversion (Figure 4, Figure S15, S19, and Table S3). Therefore, considering the syngas conversion results, it is proposed that the unique structure of RhFe alloy supported over Fe^{II}@SiO_2, that persists under catalytic condition, is crucial for shifting the products from CH_4 to CH_3CH_2OH.

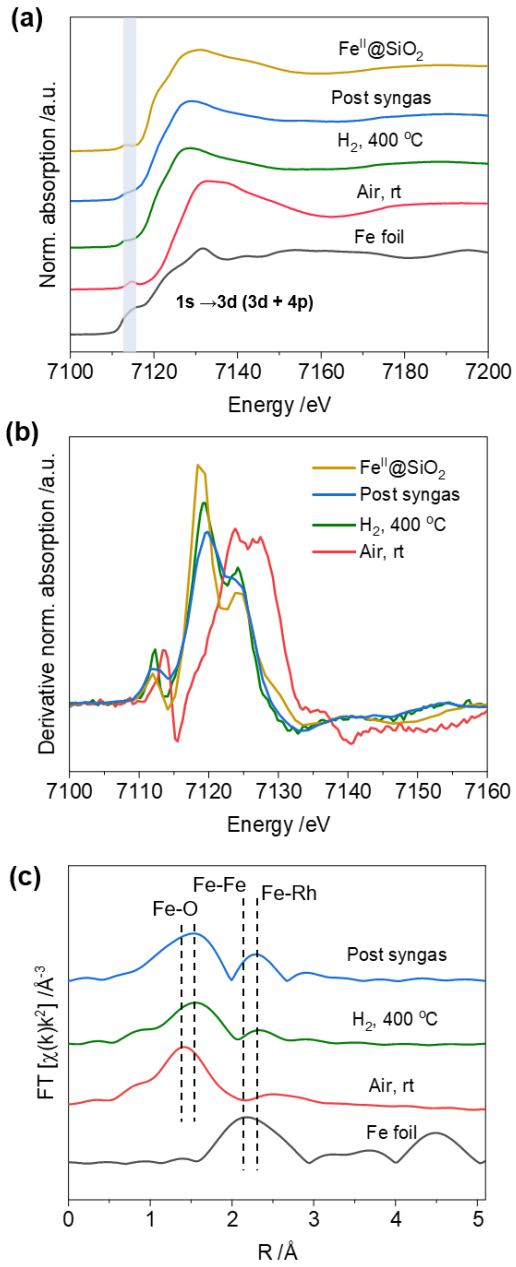

Figure 4. (a) *In situ* Fe K-edge XANES spectra for RhFe@SiO_2 under different conditions and reference samples. (b) First derivate of the EXAFS spectra at the Fe K-edge of RhFe@SiO_2 under different conditions and reference samples. (c) The k^3-weighted Fourier transforms of Fe K-edge EXAFS spectra for RhFe@SiO_2 under different conditions and reference sample.

In summary, well-defined RhFe@SiO_2 catalysts prepared via SOMC shows that Fe dramatically increases the activity in syngas conversion and shifts the selectivity of Rh from producing methane to ethanol. *In situ* XAS experiments demonstrate that ca. 20% of the overall Fe is incorporated into Rh nanoparticles after H_2 reduction, to form Rh-Fe alloy nanoparticles

with an Rh/Fe ratio of 3.3:1, while the remaining amount of Fe corresponds to Fe^{II} isolated sites dispersed on SiO_2. This structure is maintained during syngas conversion, indicating that the formation of stable RhFe alloyed nanoparticles is probably key to shift the activity/selectivity of Rh from methane to ethanol. These findings, namely, e.g. the formation of stable alloys, provide insights to design more efficient catalysts for the conversion of syngas to ethanol. Overall, this study illustrates that the combination of SOMC and advanced *in situ* spectroscopy is a powerful tool to understand the structure-performance relationship at molecular level.

Acknowledgements

This publication was created as part of NCCR Catalysis (grant number 180544), a National Center of Competence in Research funded by the Swiss National Science Foundation. C.C. and S.R.D. acknowledge the Swiss National Science Foundation (grants 200021_169134, and 200020B_192050), while C.E. acknowledges the Swiss National Science Foundation (grant 200020B_192050) and the Scholarship Fund of the Swiss Chemical Industry (SSCI). Dr. W. V. Beek and Dr. D. Stoian at the Swiss Norwegian Beamlines (SNBL, ESRF) are acknowledged for the provision of beamtime and support with *in situ* XAS experiments via proposal A31-1-168 and A31-1-222. Furthermore, ScopeM is gratefully acknowledged for their support and assistance in this work through project No. 2460 and 2658.

Conflict of interest

The authors declare no conflict of interest.

References:

[1] W. Zhou, K. Cheng, J. Kang, C. Zhou, V. Subramanian, Q. Zhang, Y. Wang, *Chem. Soc. Rev.* **2019**, *48*, 3193-3228.

[2] X. Pan, F. Jiao, D. Miao, X. Bao, *Chem. Rev.* **2021**, *121*, 6588-6609.

[3] K. T. Rommens, M. Saeys, *Chem. Rev.* **2023**, *123*, 5798-5858.

[4] G. Prieto, S. Beijer, M. L. Smith, M. He, Y. Au, Z. Wang, D. A. Bruce, K. P. de Jong, J. J. Spivey, P. E. de Jongh, *Angew. Chem. Int. Ed.* **2014**, *53*, 6397-6401.

[5] W. Zhou, J. Kang, K. Cheng, S. He, J. Shi, C. Zhou, Q. Zhang, J. Chen, L. Peng, M. Chen, Y. Wang, *Angew. Chem. Int. Ed.* **2018**, *57*, 12012-12016.

[6] J. Kang, S. He, W. Zhou, Z. Shen, Y. Li, M. Chen, Q. Zhang, Y. Wang, *Nat. Commun.* **2020**, *11*, 827.

[7] T. Lin, X. Qi, X. Wang, L. Xia, C. Wang, F. Yu, H. Wang, S. Li, L. Zhong, Y. Sun, *Angew. Chem. Int. Ed.* **2019,** 58, 4627-4631.

[8] H. Yue, X. Ma, J. Gong, *Acc. Chem. Res.* **2014**, *47*, 1483-1492.

[9] H. T. Luk, C. Mondelli, D. C. Ferré, J. A. Stewart, J. Pérez-Ramírez, *Chem. Soc. Rev.* **2017**, *46*, 1358-1426.

[10] G. Liu, G. Yang, X. Peng, J. Wu, N. Tsubaki, *Chem. Soc. Rev.* **2022**, *51*, 5606-5659.

[11] C. Wang, J. Zhang, G. Qin, L. Wang, E. Zuidema, Q. Yang, S. Dang, C. Yang, J. Xiao, X. Meng, C. Mesters, F.-S. Xiao, *Chem* **2020**, *6*, 646-657.

[12] X. Pan, Z. Fan, W. Chen, Y. Ding, H. Luo, X. Bao, *Nat. Mater.* **2007**, *6*, 507-511.

[13] S. S. Nathan, A. S. Asundi, A. S. Hoffman, J. Hong, C. Zhou, F. D. Vila, M. Cargnello, S. R. Bare, S. F. Bent, *J. Catal.* **2022**, *414*, 125-136.

[14] P. Preikschas, M. Plodinec, J. Bauer, R. Kraehnert, R. Naumann d'Alnoncourt, R. Schlögl, M. Driess, F. Rosowski, *ACS Catal.* **2021**, *11*, 4047-4060.

[15] N. Yang, A. J. Medford, X. Liu, F. Studt, T. Bligaard, S. F. Bent, J. K. Norskov, *J. Am. Chem. Soc.* **2016**, *138*, 3705-3714.

[16] R. M. Palomino, J. W. Magee, J. Llorca, S. D. Senanayake, M. G. White, *J. Catal.* **2015**, *329*, 87-94.

[17] X. Huang, D. Teschner, M. Dimitrakopoulou, A. Fedorov, B. Frank, R. Kraehnert, F. Rosowski, H. Kaiser, S. Schunk, C. Kuretschka, R. Schlogl, M. G. Willinger, A. Trunschke, *Angew. Chem. Int. Ed.* **2019**, *58*, 8709-8713.

[18] C. Coperet, A. Comas-Vives, M. P. Conley, D. P. Estes, A. Fedorov, V. Mougel, H. Nagae, F. Nunez-Zarur, P. A. Zhizhko, *Chem. Rev.* **2016**, *116*, 323-421.

[19] M. K. Samantaray, V. D Elia, E. Pump, L. Falivene, M. Hard, S. O. Chikh, L. Cavallo, J.-M. Basset, *Chem. Rev.* **2020**, *120*, 734-813.

[20] S. R. Docherty, C. Copéret, *J. Am. Chem. Soc.* **2021**, *143*, 6767-6780.

[21] S. R. Docherty, L. Rochlitz, P.-A. Payard, C. Copéret, *Chem. Soc. Rev.* **2021**, *50*, 5806-5822.

[22] L. Rochlitz, Q. Pessemesse, J. W. A. Fischer, D. Klose, A. H. Clark, M. Plodinec, G. Jeschke, P.-A. Payard, C. Copéret, *J. Am. Chem. Soc.* **2022**, *144*, 13384-13393.

[23] J. Meyet, A. Ashuiev, G. Noh, M. A. Newton, D. Klose, K. Searles, A. P. van Bavel, A. D. Horton, G. Jeschke, J. A. van Bokhoven, C. Copéret, *Angew. Chem. Int. Ed.* **2021**, *60*, 16200-16207.

[24] E. Lam, K. Larmier, P. Wolf, S. Tada, O. V. Safonova, C. Copéret, *J. Am. Chem. Soc.* **2018**, *140*, 10530-10535.

[25] S. R. Docherty, O. V. Safonova, C. Coperet, *J. Am. Chem. Soc.* **2023**, *145*, 13526-13530.

[26] P. Sot, M. A. Newton, D. Baabe, M. D. Walter, A. P. van Bavel, A. D. Horton, C. Coperet, J. A. van Bokhoven, *Chem. Eur. J.* **2020**, *26*, 8012-8016.

[27] W. Zhou, S. R. Docherty, C. Ehinger, X. Zhou, C. Copéret, *Chem. Sci.* **2023**, *14*, 5379-5385.

[28] F. Xue, W. Chen, X. Song, X. Cheng, Y. Ding, *RSC Adv.* **2016**, *6*, 35348-35353.

[29] J. Wang, Q. Zhang, Y. Wang, *Catal. Today* **2011**, *171*, 257-265

[30] M. Ichikawa, T. Fukushima, *J. Phys. Chem.* **1986**, *90*, 1222-1224.

[31] T. E. Westre, P. Kennepohl, J. G. DeWitt, B. Hedman, K. O. Hodgson, E. I. Solomon, *J. Am. Chem. Soc.* **1997**, *119*, 6297-6314.

Entry for the Table of Contents